CMS Physics Analysis Summary

Contact: cms-pag-conveners-higgs@cern.ch 2018/03/14

Search for the standard model Higgs boson in the dilepton plus photon channel in pp collisions at $\sqrt{s} = 13$ TeV

The CMS Collaboration

Abstract

A search for a Higgs boson decaying into a pair of electrons or muons plus a photon is described. This final state has contributions from Higgs decays to a Z boson and a photon ($H \to Z\gamma \to \ell\ell\gamma$, ℓ = e or μ), or to two photons, one of which has an internal conversion into a lepton pair ($H \to \gamma^*\gamma \to \mu\mu\gamma$). The analysis is performed using a dataset recorded by the CMS experiment at the LHC from proton-proton collisions at a center-of-mass energy of 13 TeV, corresponding to an integrated luminosity of 35.9 fb^{-1}. No significant excess above the background prediction has been found in the $120-130$ GeV mass range. Limits are set on the cross section for a standard model Higgs boson decaying to opposite-sign electron or muon pairs and a photon. The observed limits on cross section times the corresponding branching fractions fluctuate between 4 and 1.4 (11 and 6) times the standard model cross section for $H \to \gamma^*\gamma \to \mu\mu\gamma$ ($H \to Z\gamma \to \ell\ell\gamma$). The $H \to \gamma^*\gamma \to \mu\mu\gamma$ and $H \to Z\gamma \to \ell\ell\gamma$ analyses are combined for $m_H = 125$ GeV, obtaining an observed (expected) 95% upper limit of 3.9 (2.0) times the standard model cross section.

1 Introduction

Measurements of rare decays of the Higgs boson, such as $H \to \gamma^*\gamma$ and $H \to Z\gamma$, would enhance our understanding of the standard model (SM) of particle physics, and allow us to probe exotic couplings introduced by possible extensions of the SM [1–6]. In this paper we present a search for these decays in the leptonic channel, $(\gamma^*/Z) \to \ell\ell$ ($\ell = e, \mu$). The diagrams in Figure 1 illustrate the dominant contributions to these processes in the SM. The two processes $H \to \gamma^*\gamma \to \ell\ell\gamma$ and $H \to Z\gamma \to \ell\ell\gamma$ have the same final state and therefore interfere. Experimentally one can separate the off-shell and on-shell contributions using a selection on the invariant mass of the dilepton system, $m_{\ell\ell} = m_{(\gamma^*/Z)}$. For the purpose of this analysis we use a cut at $m_{\ell\ell} = 50\,\text{GeV}$ to separate the two processes.

It is informative to express the branching fractions for these decays relative to the $H \to \gamma\gamma$ process. In the SM, for a Higgs boson with mass $m_H = 125\,\text{GeV}$, these ratios are:

$$\frac{\Gamma(H \to \gamma^*\gamma \to \mu\mu\gamma)}{\Gamma(H \to \gamma\gamma)} = (1.69 \pm 0.25)\%, \quad \frac{\Gamma(H \to Z\gamma \to \ell\ell\gamma)}{\Gamma(H \to \gamma\gamma)} = (2.27 \pm 0.34)\%, \qquad (1)$$

where $\Gamma(H \to Z\gamma)$ and $\Gamma(H \to \gamma\gamma)$ are taken from Ref. [7], $\Gamma(H \to \gamma^*\gamma \to \mu\mu\gamma)$ is obtained with MCFM 7.0.1 [8], which is in agreement with calculations in Refs. [9–11].

The ATLAS and CMS Collaborations at the CERN LHC have both performed a search for the decay $H \to Z\gamma \to \ell\ell\gamma$ with $m_{\ell\ell} > 50\,\text{GeV}$ [12, 13] at $\sqrt{s} = 7$ and 8 TeV. The ATLAS Collaboration set an upper limit on σ/σ_{SM} of 11 at 95% confidence level (CL) for a SM Higgs boson with $m_H = 125.5\,\text{GeV}$ and the CMS Collaboration an upper limit of 9.5 at 95% CL with $m_H = 125\,\text{GeV}$. CMS has also searched for the $H \to \gamma^*\gamma \to \ell\ell\gamma$ process with $m_{\ell\ell} < 20\,\text{GeV}$ (1.5 GeV) in the dimuon (dielectron) channel at 8 TeV [14]. Combining the two channels, an upper limit of 6.7 was set on σ/σ_{SM} for $m_H = 125\,\text{GeV}$.

This paper describes the search for Higgs bosons decaying to $H \to \gamma^*\gamma \to \mu\mu\gamma$ and $H \to Z\gamma \to \ell\ell\gamma$ ($\ell = \mu$ or e). The study of the $H \to \gamma^*\gamma \to ee\gamma$ decay is challenging [14] because if

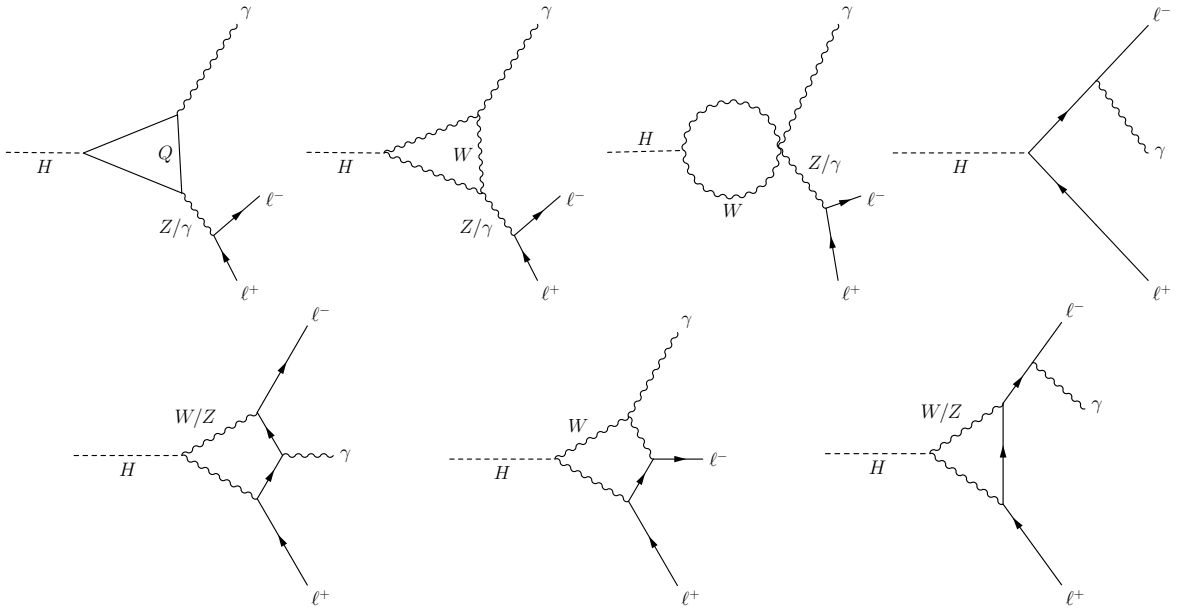

Figure 1: Dominant diagrams contributing to $H \to \ell\ell\gamma$ process.

$m_{\ell\ell}$ is low the pair of electron showers merge in the electromagnetic calorimeter (ECAL). This merging makes it difficult to trigger on such events and also to reconstruct them offline. Since there was no algorithm to resolve the merged electromagnetic deposits this channel was not included in the analysis.

The sensitivity of the search is enhanced by dividing the selected events into mutually exclusive classes according to the expected mass resolution and the signal-to-background ratio, and then combining the results from each class. The analysis uses a data sample of proton-proton collisions at a center-of-mass energy of 13 TeV recorded by the CMS experiment during 2016 corresponding to an integrated luminosity of 35.9 fb^{-1}.

2 CMS detector and trigger

A detailed description of the CMS detector can be found in Ref. [15]. The central feature of the CMS apparatus is a superconducting solenoid, 13 m in length and 6 m in diameter, which provides an axial magnetic field of 3.8 T. Within the field volume there are several particle detection systems. Charged particle trajectories are measured by silicon pixel and silicon strip trackers, covering $0 \leq \phi \leq 2\pi$ in azimuth and $|\eta| < 2.5$ in pseudorapidity. A lead-tungstate crystal electromagnetic calorimeter, ECAL, and a brass/scintillator hadron calorimeter surround the tracking volume and cover the region $|\eta| < 3$. They provide energy measurements of photons, electrons and hadron jets. The ECAL is partitioned into a barrel region with $|\eta| < 1.48$ and two endcaps that extend up to $|\eta| = 3$. A lead/silicon-strip preshower detector is located in front of the endcap of the electromagnetic calorimeter. Muons are identified and measured in gas-ionization detectors embedded in the steel return yoke outside the solenoid. The detector is nearly hermetic, allowing energy balance measurements in the plane transverse to the beam direction.

A two-tier trigger system selects collision events of interest for physics analysis. The trigger used in the $\text{H} \to \gamma^*\gamma \to \mu\mu\gamma$ channel requires a muon and a photon with transverse momentum, p_T, greater than 17 GeV and 30 GeV, respectively. The trigger efficiency is determined using signal events in simulation and $\mu\mu\gamma$ events in data. For events satisfying the selection criteria described in Section 3 the trigger efficiency is 83% in both cases. The $\text{H} \to \text{Z}\gamma \to \ell\ell\gamma$ events are required to pass at least one of the dielectron or dimuon triggers. The dielectron trigger requires a leading (subleading) electron with p_T greater than 23 (12) GeV. The dimuon trigger requires a leading (subleading) muon with p_T greater than 17 (8) GeV. The efficiencies of these dilepton triggers, for events satisfying the selection criteria are measured to be 90–98% and 93–95% for the eeγ and $\mu\mu\gamma$ channels, respectively.

3 Event selection

Events are required to have at least one good primary vertex, with reconstructed longitudinal position within 24 cm of the geometric center of the detector and transverse position within 2 cm of the beam interaction region. Due to the high instantaneous luminosity of the LHC, there are multiple p-p interactions per bunch crossing (pileup). In the case of multiple vertices, the vertex with the largest value of summed physics-object p_T^2 is taken to be the primary pp interaction vertex. The physics objects chosen are those that have been defined using information from the tracking detector, including jets, the associated missing transverse momentum, which is defined as the negative vector sum of the p_T of those jets, and charged leptons. All leptons, which are used to select events, are required to have transverse and longitudinal impact parameters with respect to the primary vertex smaller than 5 mm and 10 mm respectively.

The particle-flow (PF) event reconstruction algorithm [16] reconstructs and identifies each individual particle using an optimized combination of information from the various sub-detectors of the CMS detector.

Photon candidates are reconstructed from clusters of crystals in the ECAL with significant energy deposits. Clusters are grouped into superclusters to recover the energy from electron bremsstrahlung and photons converting in the tracker. In the endcaps, the preshower energy is also included for the region covered by the preshower ($1.65 < |\eta| < 2.6$). The clustering algorithms result in almost complete recovery of the energy of photons. Photon candidates are selected with a multivariate discriminant that uses, as inputs, isolation variables, the ratio of the energy in the hadron calorimeter behind an electromagnetic supercluster to the supercluster energy, and the transverse width of the electromagnetic shower. Isolation variables are based on particle candidates from the PF algorithm. A conversion-safe electron veto [17] is applied to avoid misidentifying an electron as a photon. This vetoes events that have a charged particle track with a hit in the inner layer of the pixel detector that points to the photon cluster in the ECAL unless that track is matched to a conversion vertex. Photons are required to lie in the geometrical region $|\eta| < 2.5$ and have $p_{\mathrm{T}} > 15\,\mathrm{GeV}$. The efficiency of the photon identification is measured from $\mathrm{Z} \to \mathrm{ee}$ events using tag-and-probe techniques [18]. It is found to be between 84 and 91% (77 and 94%) in the barrel (endcaps) after including the electron veto inefficiencies measured with $\mathrm{Z} \to \mu\mu\gamma$ events, where the photon is produced by final-state radiation.

Electron reconstruction starts from superclusters in the ECAL, which are matched to hits in the silicon strip and the pixel detectors. The energy of electrons is determined from a combination of the electron momentum at the main interaction vertex and the energy of the corresponding ECAL cluster. Electrons are selected using a multivariate discriminant that includes observables sensitive to the presence of bremsstrahlung along the electron trajectory, the geometrical and momentum-energy matching between the electron trajectory and the energy of the associated cluster in the ECAL, the shape of the electromagnetic shower in the ECAL, and the variables that discriminate against electrons originating from photon conversions [19]. In this analysis, we accept electrons with $p_{\mathrm{T}} > 7\,\mathrm{GeV}$ and $|\eta| < 2.5$.

Muon candidates are reconstructed in the tracker and identified by the PF algorithm using hits in the tracker and the muon systems. The matching between the inner and outer tracks proceeds either outside-in, starting from a track in the muon system, or inside-out, starting from a track in the silicon tracker. In the latter case, tracks that match track segments in only one or two planes of the muon system are also considered in the analysis in order to collect very low-p_{T} muons that may not have sufficient energy to penetrate the entire muon system. The muons are selected from the reconstructed muon track candidates by applying minimal requirements on the track in both the muon system and inner tracker system, and taking into account compatibility with small energy deposits in the calorimeters. We accept muons with $p_{\mathrm{T}} > 4\,\mathrm{GeV}$ and $|\eta| < 2.4$ [19].

The relative isolation variable, used to select prompt leptons, is defined as:

$$\mathcal{I}^{\ell} \equiv \left(\sum p_{\mathrm{T}}^{\mathrm{charged}} + \max\left[0, \sum p_{\mathrm{T}}^{\mathrm{neutral}} + \sum p_{\mathrm{T}}^{\gamma} - p_{\mathrm{T}}^{\mathrm{PU}}(\ell)\right] \right) / p_{\mathrm{T}}^{\ell}, \tag{2}$$

and is required to be less than 0.35, where $\sum p_{\mathrm{T}}^{\mathrm{charged}}$ is the scalar sum of the transverse momenta of charged hadrons originating from the primary vertex, $\sum p_{\mathrm{T}}^{\mathrm{neutral}}$ and $\sum p_{\mathrm{T}}^{\gamma}$ are the scalar sums of the transverse momenta for neutral hadrons and photons, respectively. The isolation sums are performed over a cone of angular radius $\Delta R = 0.3$ ($\Delta R \equiv \sqrt{(\Delta\phi)^2 + (\Delta\eta)^2}$) around the lepton direction at the primary vertex. For muons, $p_{\mathrm{T}}^{\mathrm{PU}}(\mu) \equiv 0.5 \sum_i p_{\mathrm{T}}^{\mathrm{PU},i}$, where i runs over

the momenta of the charged hadron PF candidates not originating from the primary vertex. For electrons, $p_{\mathrm{T}}^{\mathrm{PU}}(\mathrm{e}) \equiv \rho\, A_{\mathrm{eff}}$, where the effective area A_{eff} is a coefficient that is dependent on electron η and is chosen in such a way that the isolation efficiency is independent of pileup, and ρ is the median of the p_{T} density distribution for neutral particles. Finally, p_{T}^{ℓ} is the transverse momenta of the selected lepton. To suppress muons originating from in-flight decays of hadrons and electrons from photon conversions, we require each lepton track to have a 3D impact parameter with respect to the primary vertex that is less than 4 times its uncertainty.

The electron selection criteria, including the isolation requirement, are optimized to maintain an efficiency of approximately 85-93 (81-92)% in the barrel (endcap) for electrons from W or Z decays. For muons, the identification is tuned to maintain efficiency at low ΔR where the two muons are close to each other. The identification and isolation efficiency for single muons from $Z \to \mu\mu$ or J/ψ decays is 85-97 (88-96)% in the barrel (endcap). In case of the $\mathrm{H} \to \gamma^*\gamma \to \mu\mu\gamma$, the $\Delta R(\mu\mu)$ between the two muons is small due to their low invariant mass and the high p_{T} of the γ^*. Hence, no isolation requirement is applied to the subleading muons as they are within the isolation cone of the leading muons in most events. The identification efficiency of muons from γ^* is $\sim$ 94-98 (92-97)% in the barrel (endcap).

Selected events are classified into classes described in detail below. The dijet-tagged and boosted jet event classes use jets that are built by clustering the PF candidates using the anti-$\mathrm{k_T}$ clustering algorithm with distance parameter $R = 0.4$ in the FASTJET software package [20]. Only charged PF candidates associated with the primary vertex are used in the jet clustering procedure. In situ measurements of the momentum balance in dijet, photon + jet, Z+jet, and multijet events are used to account for any residual differences in jet energy scale in data and simulation. Additional selection criteria are applied to each event to remove spurious jet-like features originating from isolated noise patterns in certain HCAL regions. Calibrated and corrected jets are required to have transverse energy greater than 30 GeV and $|\eta| < 4.7$, and to be separated by at least 0.4 in ΔR from leptons and photons passing the selection requirements described above.

3.1 $\mathrm{H} \to \gamma^*\gamma \to \mu\mu\gamma$ selection

In the $\mathrm{H} \to \gamma^*\gamma \to \mu\mu\gamma$ search we select events with two muons and a photon, where the muons must have opposite charge and $p_{\mathrm{T}} > 20\,(4)$ GeV for the leading (subleading) lepton. The p_{T} requirement on the leading muon is driven by the trigger threshold, and that on the subleading muon by the minimum energy needed to reach the muon system. The photon and dilepton momenta both must satisfy $p_{\mathrm{T}} > 0.30 \cdot m_{\mu\mu\gamma}$, where $m_{\mu\mu\gamma}$ is the invariant mass of $\mu\mu\gamma$ system. The separation between each muon and the photon is required to satisfy $\Delta R > 1$ in order to suppress Drell–Yan background events with final-state radiation.

The dimuon invariant mass is required to be less than 50 GeV to make this selection and the $\mathrm{Z}\gamma$ selection described in Section 3.2 mutually exclusive. Events with a dimuon mass in the ranges $2.9 < m_{\mu\mu} < 3.3$ GeV and $9.3 < m_{\mu\mu} < 9.7$ GeV are rejected to avoid $\mathrm{J}/\psi \to \mu\mu$ and $\Upsilon \to \mu\mu$ contamination. The invariant mass $m_{\mu\mu\gamma}$ is required to satisfy $110 < m_{\mu\mu\gamma} < 170$ GeV.

A variable R_9 is defined as the energy sum of the 3×3 ECAL crystals centered on the most energetic crystal in the supercluster divided by the energy of the supercluster. The selected events are separated into four mutually exclusive event classes based on the R_9 and η of the photon and the presence of jets. An R_9 value of 0.94 is used to separate the reconstructed photons into two regions. The region containing unconverted photons, with larger values of R_9 and better energy resolution, has a smaller background. By separating events into two regions of low/high R_9 value, the sensitivity of the analysis is increased. We therefore have the

following categories: photon in the barrel region (EB) with a high R_9 value; photon in the barrel with low R_9 value; photon in the endcap regions (EE); and events that require the presence of at least two jets passing the selection criteria described below. Only events that do not pass the dijet tag are included in the EB or EE classes. By using this event classification scheme, as opposed to combining all events in one class, the sensitivity of this analysis is increased by 11%.

For the dijet-tagged event class the two highest transverse energy jets are used and the requirements for this class are: (i) the difference in pseudorapidity between the two jets is greater than 3.5; (ii) the Zeppenfeld variable ($\eta_{\ell\ell\gamma} - (\eta_{j1} + \eta_{j2})/2$) is less than 2.5, where $\eta_{\ell\ell\gamma}$ is the η of the $\ell\ell\gamma$ system, η_{j1} and η_{j2} are the pseudo-rapidities of the leading and sub-leading jets; (iii) the dijet mass is greater than 500 GeV; and (iv) the difference in azimuthal angles between the dijet system and the $\ell\ell\gamma$ system is greater than 2.4. These cuts mainly target the VBF production mechanism of the Higgs.

The resulting acceptance times efficiency for $\mathrm{pp} \to \mathrm{H} \to \gamma^*\gamma \to \mu\mu\gamma$ is between 26 and 27% for m_H between 120 and 130 GeV.

3.2 $\mathrm{H} \to \mathrm{Z}\gamma \to \ell\ell\gamma$ selection

In the $\mathrm{H} \to \mathrm{Z}\gamma \to \ell\ell\gamma$ search, events with a photon and with two same-flavor leptons (e or μ) consistent with a Z-boson decay are selected. All particles must be isolated and have p_T greater than 25 (15) GeV for the leading (subleading) electron; 20 (10) GeV for the leading (subleading) muon and 15 GeV for the photon. In the rare cases where there are multiple dilepton pairs in the event, the one with the mass closest to the Z boson nominal mass is selected. The invariant mass of the selected pair is required to be larger than 50 GeV. This ensures that the $\mathrm{H} \to \mathrm{Z}\gamma \to \ell\ell\gamma$ event selection is orthogonal to that for $\mathrm{H} \to \gamma^*\gamma \to \mu\mu\gamma$.

The events are required to have photon $E_\mathrm{T} > 0.14 \cdot m_{\ell\ell\gamma}$, which rejects backgrounds without significant loss in signal sensitivity and without introducing a bias in the $m_{\ell\ell\gamma}$ spectrum. Leptons are required to have $\Delta R > 0.4$ with respect to the photon in order to reject events with initial-state radiation. In addition, we require $m_{\ell\ell\gamma} + m_{\ell\ell} > 185$ GeV to reject events with final-state radiation from Drell–Yan processes. Finally, the invariant mass of the $\ell\ell\gamma$ system is required to be $100 < m_{\ell\ell\gamma} < 180$ GeV.

The selected events are classified into the mutually exclusive classes. A lepton-tag class contains events with an additional electron with $p_\mathrm{T} > 7$ GeV or a muon with $p_\mathrm{T} > 5$ GeV, to target Higgs boson production in association with either a Z or W boson. Events not included in the lepton class are considered for the dijet class. In this case the criteria described in Section 3.1 are used to select events containing a dijet, targeting Higgs boson production in a VBF process. The next class considered is the boosted class, which contains events where the transverse momentum of the $\ell\ell\gamma$ system is greater than 60 GeV, to enhance the fraction of events that contain a boosted Higgs boson recoiling against a jet. Events that do not fall into these three classes are placed in the untagged categories. A significant fraction of the signal events are expected to have both leptons and the photon in the barrel, while only a sixth of the signal events have the photon in the endcap. This is in contrast to the background, where fewer than half of the events are in the barrel, while at least a third have a photon in the endcap. Furthermore, events where the photon does not convert to $\mathrm{e}^+\mathrm{e}^-$ have a smaller fraction of background and better resolution. For these reasons, the untagged events are classified into four categories according to the pseudorapidity of the leptons and photon and the R_9 value of the photon as seen in Table 1.

Table 1: Categories in $H \to Z\gamma \to \ell\ell\gamma$.

Category	$e^+e^-\gamma$	$\mu^+\mu^-\gamma$
Lepton tagged	additional electron ($p_T > 7$ GeV) or muon ($p_T > 5$ GeV)	
Di-jet tagged	at least 2 jets required	–same–
Boosted tagged	p_T of $\ell\ell\gamma > 60$ GeV	–same–
untagged 1	Photon $0 < \lvert\eta\rvert < 1.4442$ Both leptons $0 < \lvert\eta\rvert < 1.4442$ $R_9 > 0.94$	Photon $0 < \lvert\eta\rvert < 1.4442$ Both leptons $0 < \lvert\eta\rvert < 2.1$ and one lepton $0 < \lvert\eta\rvert < 0.9$ $R_9 > 0.94$
untagged 2	Photon $0 < \lvert\eta\rvert < 1.4442$ Both leptons $0 < \lvert\eta\rvert < 1.4442$ $R_9 < 0.94$	Photon $0 < \lvert\eta\rvert < 1.4442$ Both leptons $0 < \lvert\eta\rvert < 2.1$ and one lepton $0 < \lvert\eta\rvert < 0.9$ $R_9 < 0.94$
untagged 3	Photon $0 < \lvert\eta\rvert < 1.4442$ At least one lepton $1.4442 < \lvert\eta\rvert < 2.5$ none between $1.4442 < \lvert\eta\rvert < 1.566$ No requirement on R_9	Photon $0 < \lvert\eta\rvert < 1.4442$ Both leptons in $\lvert\eta\rvert > 0.9$ or one lepton in $2.1 < \lvert\eta\rvert < 2.4$ No requirement on R_9
untagged 4	Photon $1.566 < \lvert\eta\rvert < 2.5$ Both leptons $0 < \lvert\eta\rvert < 2.5$ none between $1.4442 < \lvert\eta\rvert < 1.566$ No requirement on R_9	Photon $1.566 < \lvert\eta\rvert < 2.5$ Both leptons $0 < \lvert\eta\rvert < 2.4$ No requirement on R_9

It should be noted that the electron and muon channels are considered separately in all classes except for the lepton class where the number of events is small. This event classification scheme increases the sensitivity of the analysis by 18%. The resulting acceptance times efficiency for $pp \to H \to Z\gamma \to \ell\ell\gamma$ in the electron (muon) channel is between 18 and 24% (25 and 31%) for m_H between 120 and 130 GeV.

A complete list of all the categories considered in the analysis ($pp \to H \to \gamma^*\gamma \to \mu\mu\gamma$ and $pp \to H \to Z\gamma \to \ell\ell\gamma$), together with the expected yields for a 125 GeV standard model Higgs signal, are shown in Table 2. This table also reports yields from signal processes gluon-gluon fusion (ggH), vector boson fusion (VBF), associated VH production (VH) and Higgs production in association with top quarks (ttH).

4 Signal and background modeling

The search for signal in this paper is performed using a shape-based analysis. The background is estimated from data and the signal is estimated using the simulation. Even though the background is estimated from data, simulated samples are used in the $H \to Z\gamma \to \ell\ell\gamma$ search to optimize the event classes. The main background, $pp \to Z\gamma$, is generated at next-to-leading order (NLO) using the MADGRAPH5_AMC@NLO 2.3.3 generator [21]. The $Z(\ell\ell)$+jets events with a jet misidentified as a photon are another important source of background, and are generated at NLO using MADGRAPH5_AMC@NLO. All background events are interfaced to PYTHIA 8.205 for the fragmentation and hadronization of partons.

Signal samples for the $H \to \gamma^*\gamma \to \mu\mu\gamma$ processes in gluon fusion (ggH), vector boson fusion (VBF), and production in association with a W/Z (VH) are simulated at next-to-leading order (NLO) using the MADGRAPH5_AMC@NLO matrix-element generator [21], with the Higgs characterization model [22, 23], interfaced with PYTHIA 8.212 [24] for parton showering and hadronization. Higgs boson production in association with a $t\bar{t}$ pair makes a negligible contribution to the signal and is ignored. For the $H \to Z\gamma$ process, the simulated

Table 2: Expected signal yields for a 125 GeV SM Higgs boson for all the categories in $H \to \gamma^*\gamma \to \mu\mu\gamma$ and $H \to Z\gamma \to \ell\ell\gamma$, in the narrowest mass window around 125 GeV containing 68.3% of the expected signal distribution.

Analysis	Channel	Category	Number of signal events for $m_H = 125$ GeV		
			ggH	VBF	VH+ttH
$H \to \gamma^*\gamma \to \mu\mu\gamma$	$\mu\mu$	EB, High R_9	9.18	0.47	0.33
	$\mu\mu$	EB, Low R_9	5.17	0.27	0.18
	$\mu\mu$	EE	3.80	0.20	0.25
	$\mu\mu$	dijet	0.45	0.39	0.01
$H \to Z\gamma \to \ell\ell\gamma$	ee	untagged 1	5.2	0.14	0.06
	ee	untagged 2	3.2	0.09	0.04
	ee	untagged 3	3.9	0.12	0.06
	ee	untagged 4	2.7	0.08	0.04
	$\mu\mu$	untagged 1	7.3	0.22	0.09
	$\mu\mu$	untagged 2	4.6	0.14	0.06
	$\mu\mu$	untagged 3	3.9	0.12	0.06
	$\mu\mu$	untagged 4	3.4	0.11	0.05
	ee	dijet	0.33	0.47	0.02
	$\mu\mu$	dijet	0.43	0.60	0.02
	ee	boosted	3.36	0.56	0.33
	$\mu\mu$	boosted	4.37	0.72	0.43
	ee + $\mu\mu$	lepton	0.08	0.014	0.32

events from all four production processes (ggH, VBF, VH and ttH) are generated at NLO using POWHEG [25, 26], interfaced with PYTHIA 8.212 [24]. The NLO parton distribution function (PDF) set, NNPDF3.0 [27], is used to produce these samples. The SM Higgs boson production cross sections and branching ratios recommended by the LHC Higgs cross section working group [7] are used for $H \to Z\gamma$, whereas, for $H \to \gamma^*\gamma$, the production cross sections are also taken from Ref. [7], but the branching ratio is taken from MCFM and given in Equation 1.

The simulated signal events are re-weighted by taking into account the difference between data and simulated events so that the distribution of pileup vertices, the trigger efficiencies, the resolution, the energy scale, the reconstruction efficiencies and the isolation efficiency – for electrons, muons and photons – observed in data are reproduced. An additional correction is applied to photons to reproduce the performance of the R_9 shower shape variable.

The dominant backgrounds to $H \to \ell\ell\gamma$ consist of the irreducible non-resonant SM $\ell\ell\gamma$ production, and of final-state radiation in Z decays and γ^* conversions, and of Drell-Yan production in association with jets, where a jet or a lepton is misidentified as a photon.

The background is estimated from data, by fitting the observed $\ell\ell\gamma$ mass distributions. Separate fits are performed to the four event classes for the $H \to \gamma^*\gamma \to \mu\mu\gamma$ analysis and the thirteen classes for the $H \to Z\gamma \to \ell\ell\gamma$. For the $H \to \gamma^*\gamma \to \mu\mu\gamma$ analysis the range $110 < m_{\ell\ell\gamma} < 170$ GeV is used in the fit and for the $H \to Z\gamma \to \ell\ell\gamma$ analysis the range $115 < m_{\ell\ell\gamma} < 180$ GeV is used. The fit model of the signal is obtained from an unbinned fit to the mass distribution of the corresponding sample of simulated events to a Crystal Ball function [28] plus a Gaussian function. To derive the signal shapes for the intermediate mass points where simulation was not available, a linear interpolation of the fitted parameters for available mass points was performed.

The choice of the background fit function is based on a study that minimizes the bias which

might be introduced by the selected function. The study of the bias is performed for four families of functions. Pseudo-data is generated from background-only fits to the observed $m_{\ell\ell\gamma}$ spectrum for:

1. A sum of N exponential functions
$$\sum_{i=1}^{N} f_i e^{p_i m_{\ell\ell\gamma}} \tag{3}$$
with $2N$ free parameters: $p_i < 0$ and f_i. The lowest order considered has $N = 1$.

2. A sum of N power-functions
$$\sum_{i=1}^{N} f_i m_{\ell\ell\gamma}^{p_i} \tag{4}$$
with $2N$ free parameters $p_i < 0$ and f_i. The lowest order considered has $N = 1$.

3. Bernstein polynomials of N^{th} order, with N=1, 2, 3, 4 and 5
$$Ber_N(m_{\ell\ell\gamma}) = \sum_{i=1}^{N} f_i^2 \binom{N}{i} m_{\ell\ell\gamma}^i (1 - m_{\ell\ell\gamma})^{N-i} \tag{5}$$
with N free parameters f_i.

4. Laurent series with N=2, 3 and 4 terms
$$f_2 m_{\ell\ell\gamma}^{-4} + f_3 m_{\ell\ell\gamma}^{-5}\,, \tag{6}$$
$$f_1 m_{\ell\ell\gamma}^{-3} + f_2 m_{\ell\ell\gamma}^{-4} + f_3 m_{\ell\ell\gamma}^{-5}\,, \tag{7}$$
and
$$f_1 m_{\ell\ell\gamma}^{-3} + f_2 m_{\ell\ell\gamma}^{-4} + f_3 m_{\ell\ell\gamma}^{-5} + f_4 m_{\ell\ell\gamma}^{-6}\,, \tag{8}$$
with N free parameters $f_{1\cdots4}$.

A test is then performed to determine the best order in each family. In this test, the difference in the negative log-likelihood between fits performed with two different orders of the same family of functions, N and N+1, indicates whether the data supports the hypothesis of the higher-order function. A p-value of this quantity is then calculated as:

$$p - \text{value} = Prob(2\Delta NLL > 2\Delta NLL_{N+1} | \chi^2(M)), \tag{9}$$

where ΔNLL is the difference of log-likelihood between the two fits; $\Delta NLL_{N+1} = 2(NLL_N - NLL_{N+1})$ follows a χ^2 distribution with M degrees of freedom where M is the difference in the number of free parameters between the N+1 function and N function. If the p-value is less than 0.05, the higher order function is supported by the data and the procedure is then applied to the higher order functions in the family. The procedure stops when the p-value becomes greater than 0.05.

Once the best order of each family is determined for each category, pseudo-experiments (with no injected signal) describing possible experimental outcomes are randomly generated using

each of the determined functions as generators of background. Each of these sets of pseudo-experiments are fitted with all the other functions, in order to determine the presence of a possible bias introduced by the fitting function. In each fit, the bias is estimated with a pull variable, computed as $(\mu_{FIT} - \mu_t)/\sigma_{FIT}$, where μ_{FIT} and σ_{FIT} are the mean and the standard deviation of the signal strength determined from the fit, and μ_t is the true injected signal strength. A given fit function is deemed acceptable in a given category if its pull is less than 14% of the statistical uncertainty when fitting pseudo-experiments generated with all of the other functional families. Table 3 shows the fit functions chosen in each category of the analysis.

Table 3: Fit function chosen as a result of the bias study used in the analysis.

$m_{\ell\ell}$	Category	Best fit function
< 50 GeV	EB - low R_9	Bernstein of order 4
	EB - high R_9	Bernstein of order 4
	EE	Bernstein of order 4
	Dijet tag	Exponential of order 2
> 50 GeV	Untagged 1	Bernstein of order 4
	Untagged 2	Bernstein of order 5
	Untagged 3	Bernstein of order 4
	Untagged 4	Bernstein of order 4
	Dijet tag	Power law of order 1
	Boosted tag	Bernstein of order 3
	Lepton tag	Power law of order 1

The background fits based on the $m_{\ell\ell\gamma}$ data distributions for the event categories of the $H \to \gamma^*\gamma \to \mu\mu\gamma$ analysis are shown in Figure 2 and for the electron and muon channels in all $H \to Z\gamma \to \ell\ell\gamma$ event class definitions in Figure 3 and Figure 4 respectively. Finally, Figure 5 shows the background fit for the lepton tag category in the $H \to Z\gamma \to \ell\ell\gamma$ analysis.

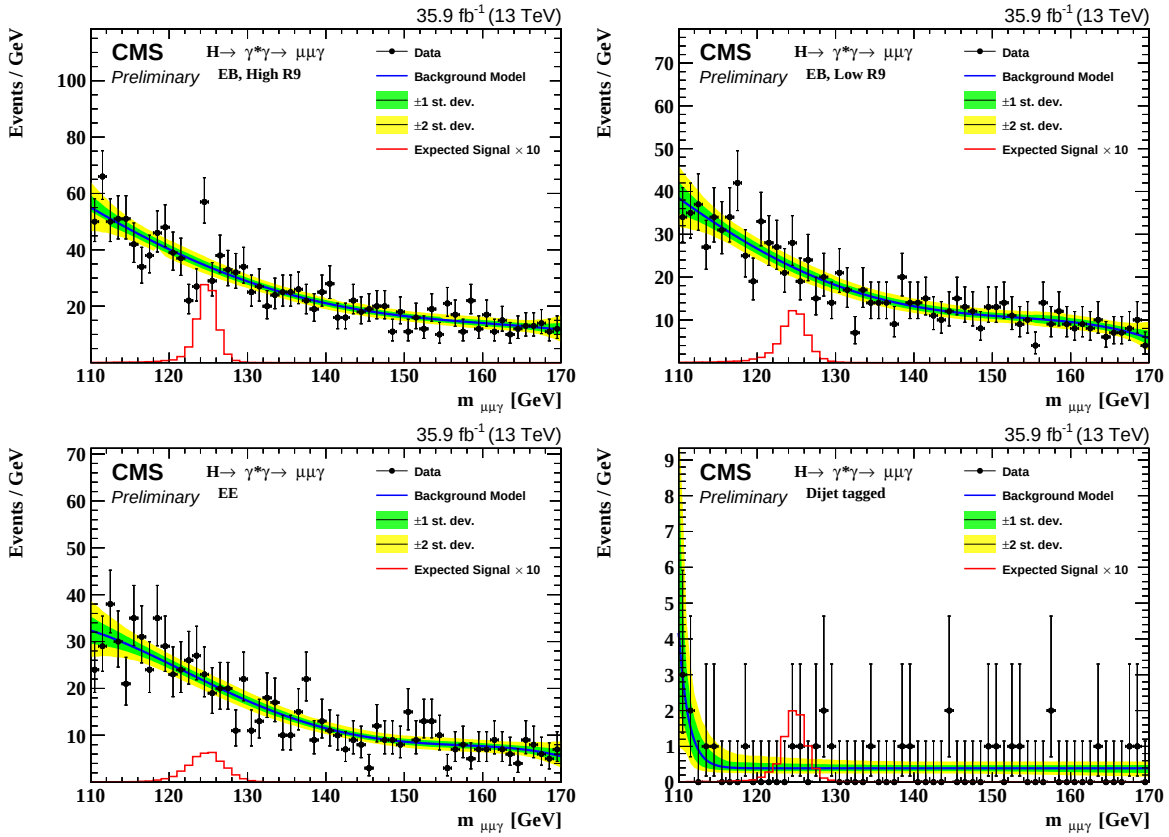

Figure 2: Background model fit to the $m_{\mu\mu\gamma}$ distribution for all event classes for the $\mathrm{H} \to \gamma^*\gamma \to \mu\mu\gamma$ selection. The green and yellow bands represent the 68% and 95% uncertainties in the fit to the data.

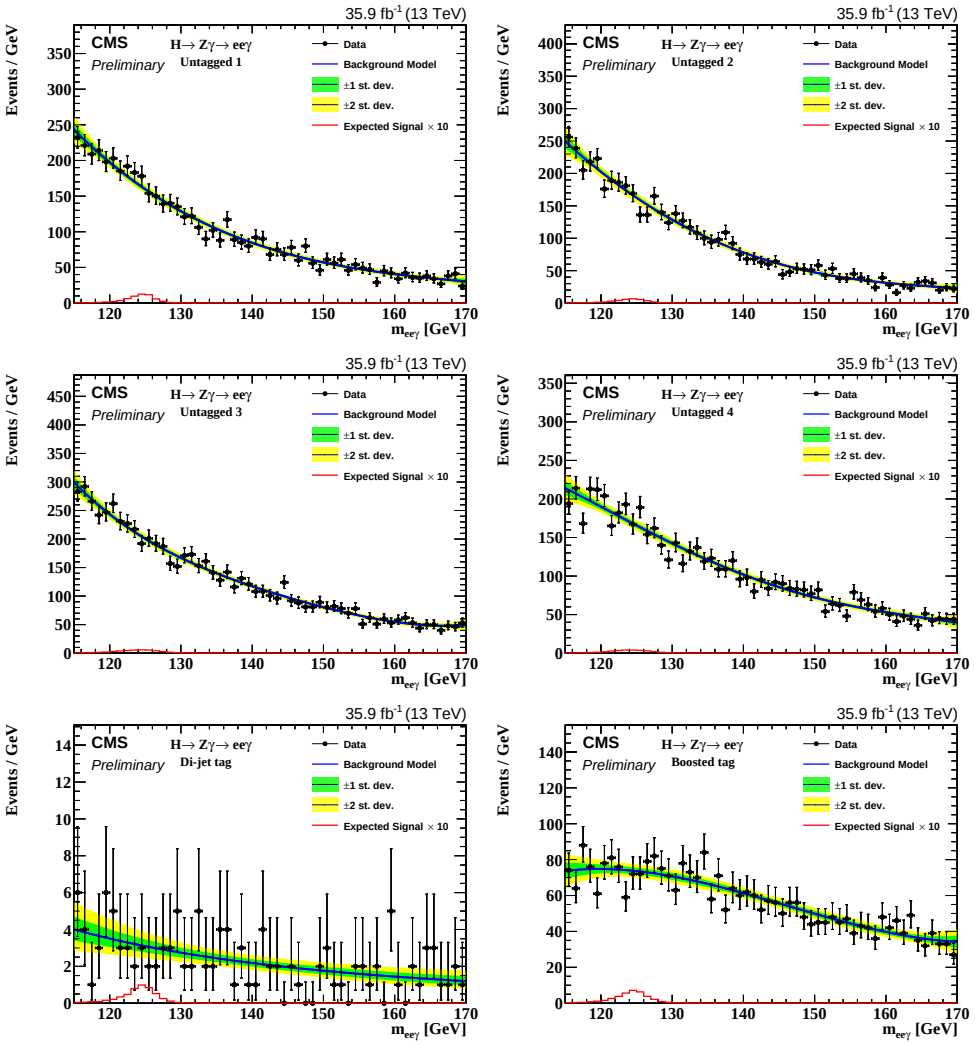

Figure 3: Background model fit to the $m_{ee\gamma}$ distribution for untagged 1 (top left), untagged 2 (top right), untagged 3 (middle left), untagged 4 (middle right), di-jet tagged (bottom left) and boosted tag (bottom right) for the $H \rightarrow Z\gamma \rightarrow ee\gamma$ selection. The green and yellow bands represent the 68% and 95% uncertainties in the fit to the data.

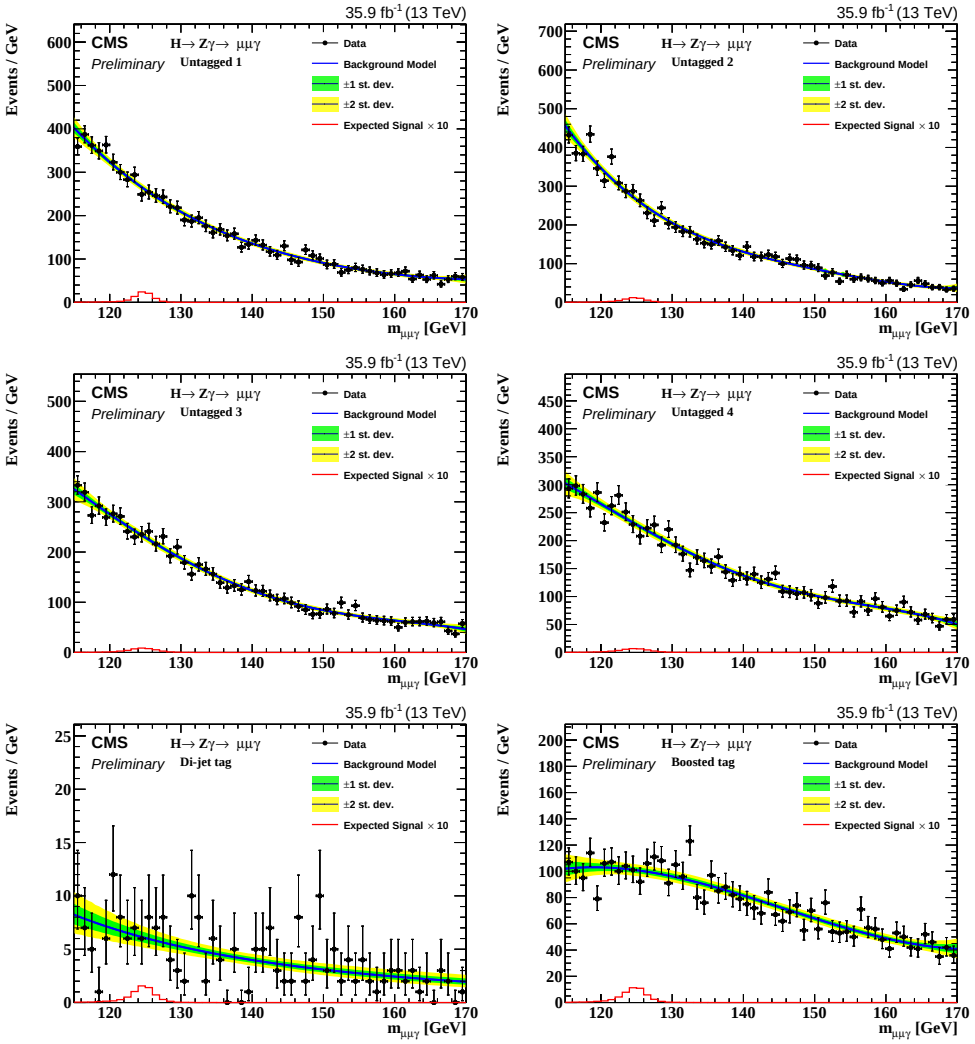

Figure 4: Background model fit to the $m_{\mu\mu\gamma}$ distribution for untagged 1 (top left), untagged 2 (top right), untagged 3 (middle left), untagged 4 (middle right), di-jet tagged (bottom left) and boosted tag (bottom right) for the $H \to Z\gamma \to \mu\mu\gamma$ selection. The green and yellow bands represent the 68% and 95% uncertainties in the fit to the data.

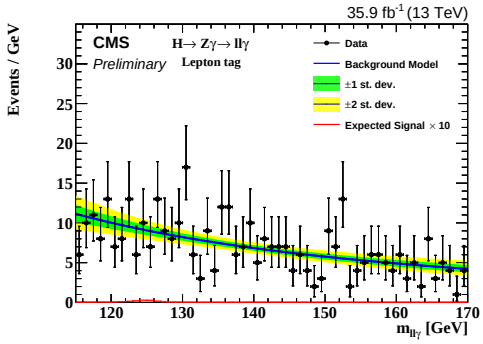

Figure 5: Background model fit to the $m_{\ell\ell\gamma}$ distribution for $H \to Z\gamma \to \ell\ell\gamma$ lepton tag category. The green and yellow bands represent the 68% and 95% uncertainties in the fit to the data.

5 Results

No deviation from the background-only hypothesis is observed, and the data are used to derive upper limits on the Higgs boson production cross section times the branching fractions, $\sigma(\mathrm{pp} \to \mathrm{H})\,\mathcal{B}(\mathrm{H} \to \gamma^*\gamma \to \mu\mu\gamma)$ and $\sigma(\mathrm{pp} \to \mathrm{H})\,\mathcal{B}(\mathrm{H} \to \mathrm{Z}\gamma \to \ell\ell\gamma)$, divided by the corresponding SM predictions. The limits are evaluated using a modified frequentist approach, CL_S, taking the profile likelihood as a test statistic [29–31]. An unbinned evaluation of the likelihood is considered.

Background uncertainties in this analysis are taken from the fit to the data. As for the uncertainties related to the signal yield, the following sources of systematic uncertainties are considered:

- Electron and photon energy scale/resolution. The electromagnetic scale is known with 0.15-0.5% (1%) precision in EB (EE). To quantify this uncertainty, the electron energy and photon energy are varied and the effect on signal mean/resolution is propagated as a shape nuisance in the estimation of limits.
- Muon momentum scale/resolution. The uncertainty in muon momentum scale is 1%. To quantify this uncertainty, the muon momentum scale is varied and the effect on signal mean/resolution is propagated as a shape nuisance in the estimation of limits.
- Luminosity. The uncertainty in the CMS integrated luminosity is 2.5% [32].
- Object ID and isolation. The corrections applied to the simulation to reproduce the performance of the lepton and photon selection is measured with $\mathrm{Z} \to \mathrm{ee}/\mu\mu$ events.
- Pileup. The uncertainty from the description of the pileup in the signal simulation is estimated by varying the total inelastic cross section by $\pm$ 4.6%.
- Jet-energy scale/resolution. The uncertainty in the jet energy scale/ resolution is accounted for by changing the jet response/resolution by $\sim$ 2%.
- Underlying event and parton shower uncertainty. The uncertainty associated with the choice and tuning of the generator is estimated with dedicated samples which are generated with a different generator tune. The difference in signal yields with respect to the nominal configuration is propagated as the uncertainty.
- R_9 reweighting. As the distribution of this shower-shape variable in the data does not match the simulation, the R_9 distribution in the signal simulation is re-weighted to that in the data. This re-weighting introduces an uncertainty that is estimated by removing the R_9 re-weighting in the simulation and then re-estimating the yields in the categories where R_9 is used for categorization.
- Theoretical sources. These include the systematic uncertainties from the effect of the choice of parton distribution function on the signal cross section [33–36] and the uncertainty in the Higgs branching fraction prediction [7]. In case of $\mathrm{H} \to \gamma^*\gamma$ analysis, the systematics on the branching ratio was estimated by inflating the uncertainties on the branching ratio of $\mathrm{H} \to \mathrm{Z}\gamma$ to 6%.

The pre-fit values of the nuisance parameters included in the analysis, averaged over all the categories are summarized in Table 4.

Based on the fit bias studies, the uncertainty on the background estimation due to the chosen functional form is assumed to be negligible. Furthermore, to combine the $\mathrm{H} \to \mathrm{Z}\gamma \to \ell\ell\gamma$ and $\mathrm{H} \to \gamma^*\gamma \to \mu\mu\gamma$ channels, uncertainties from theoretical sources, luminosity, object ID, R_9 re-weighting, jet energy correction and resolution are considered to be correlated across the categories.

Table 4: Sources of systematic uncertainties considered in the $H \to Z\gamma \to \ell\ell\gamma$ and $H \to \gamma^*\gamma \to \mu\mu\gamma$ analyses. The pre-fit values of the nuisance parameters are shown averaged over all the categories in the analysis in the second column which either affect the normalization of the simulated signal event yields or the mean and resolution of $m_{\ell\ell\gamma}$.

Sources	$H \to Z\gamma \to \ell\ell\gamma$	$H \to \gamma^*\gamma \to \mu\mu\gamma$
Theory		
- Gluon-gluon fusion cross section (scale)	3.9%	3.9%
- Gluon-gluon fusion cross section (PDF)	3.2%	3.2%
- Vector boson fusion cross section (scale)	+0.4% -0.3%	+0.4% -0.3%
- Vector boson fusion cross section (PDF)	2.1%	2.1%
- W associate production (scale)	+0.5% -0.7%	+0.5% -0.7%
- W associate production (PDF)	1.9%	1.9%
- Z associate production (scale)	+3.8% -3.1%	+3.8% -3.1%
- Z associate production (PDF)	1.6%	1.6%
- Top pair associate production (scale)	+5.8% -9.2%	n.a.
- Top pair associate production (PDF)	3.6%	n.a.
Underlying Event/Parton Shower		
- Muon	3%	4.7%
- Electron	3%	n.a.
Branching fraction	5.7%	6%
Luminosity	2.5%	2.5%
Lepton identification (ID) and isolation		
- Muon channel	0.6%	2%
- Electron channel	1.2%	n.a.
Photon identification (ID) and isolation		
- Muon channel	2.3%	1.6%
- Electron channel	2.2%	n.a.
Pileup reweighting		
- Muon channel	0.6%	0.3%
- Electron channel	0.9%	n.a.
R_9 reweighting		
- Muon channel	6.5%	9%
- Electron channel	6.8%	n.a.
Trigger		
- Muon	1.3%	4%
- Electron	1%	n.a.
Energy/Momentum – muon channel		
- signal mean	0.04%	0.08%
- signal resolution	4%	5%
Energy – electron channel		
- signal mean	0.15%	n.a.
- signal resolution	4%	n.a.
Jet energy scale		
- Muon	2.5%	3.8%
- Electron	2.7%	n.a.
Jet energy resolution		
- Muon	0.3%	0.7%
- Electron	0.3%	n.a.

The expected and observed exclusion limits at 95% confidence level for the process $H \to \gamma^*\gamma \to \mu\mu\gamma$ are shown in Figure 6. The expected limits are between 2.3 and 2.1 times the SM cross section and the observed limit fluctuates between about 4 and 1.4 times the standard model cross section. The limits are calculated at 1 GeV intervals in the mass range of $120 < m_H <$

130 GeV. Figure 7 shows the combined limit for the $H \to Z\gamma \to \ell\ell\gamma$ channel. The expected exclusion limits at 95% confidence level are between 9 and 3.8 times the SM cross section and the observed limit fluctuates between about 11 and 6 times the SM cross section.

Finally, Figure 8 shows the expected limit for each category and the combined limit for both channels for $m_H = 125$ GeV. The combined observed (expected) limit is 3.9 (2.0) for a 125 GeV Higgs boson decaying to $\ell\ell\gamma$. After combining both the analyses, $H \to \gamma^*\gamma \to \mu\mu\gamma$ and $H \to Z\gamma \to \ell\ell\gamma$ and considering the background-only hypothesis, the observed p-value at $m_H = 125$ GeV is 0.02 which corresponds to around two standard deviations. The combined expected p-value for a SM Higgs boson at $m_H = 125$ GeV is 0.16, corresponding to a significance of around one standard deviation.

6 Summary

A search has been performed for a SM Higgs boson decaying into a dilepton and a photon. The analysis uses a dataset from proton-proton collisions at a center-of-mass energy of 13 TeV, corresponding to an integrated luminosity of 35.9 fb^{-1}. No significant excess has been found and the limits on the Higgs production cross section times the corresponding branching fractions at the LHC have been derived. The expected exclusion limits at 95% confidence level are around 2.3–2.1 (9–3) times the SM cross section in the $H \to \gamma^*\gamma \to \mu\mu\gamma$ ($H \to Z\gamma \to \ell\ell\gamma$) channel in the mass range from 120 and 130 GeV, and the observed limit fluctuates between about 4 and 1.4 (11 and 6) times the SM cross section. Finally, the $H \to \gamma^*\gamma \to \mu\mu\gamma$ and $H \to Z\gamma \to \ell\ell\gamma$ analyses have been combined for $m_H = 125$ GeV, obtaining an observed (expected) 95% upper limit of 3.9 (2.0) times the standard model cross section.

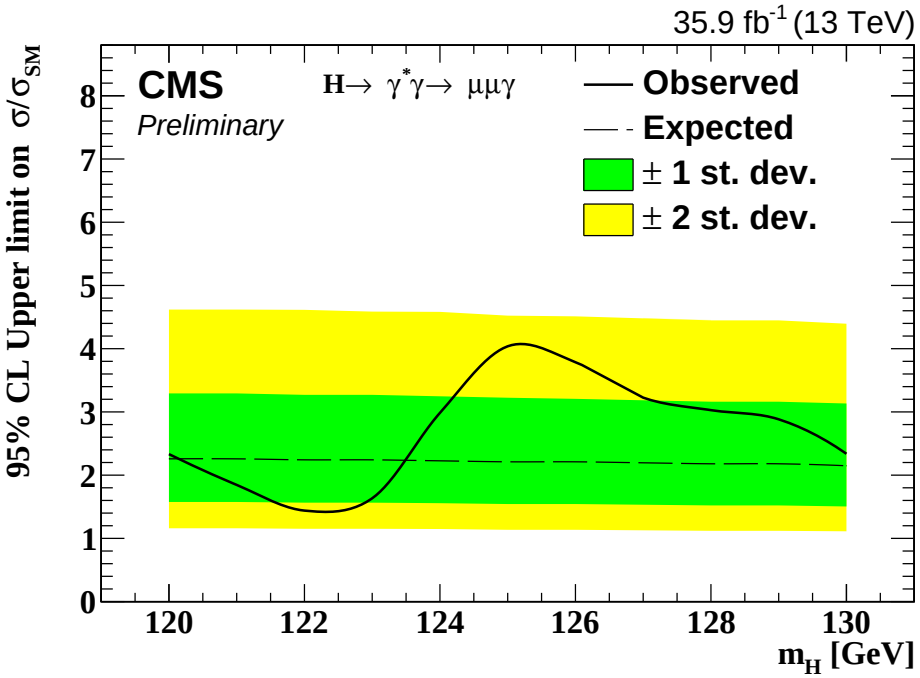

Figure 6: Exclusion limit, at 95% confidence level, on the cross section of $H \to \gamma^*\gamma \to \mu\mu\gamma$ as a function of the Higgs boson mass based on 35.9 fb^{-1} of data taken at 13 TeV.

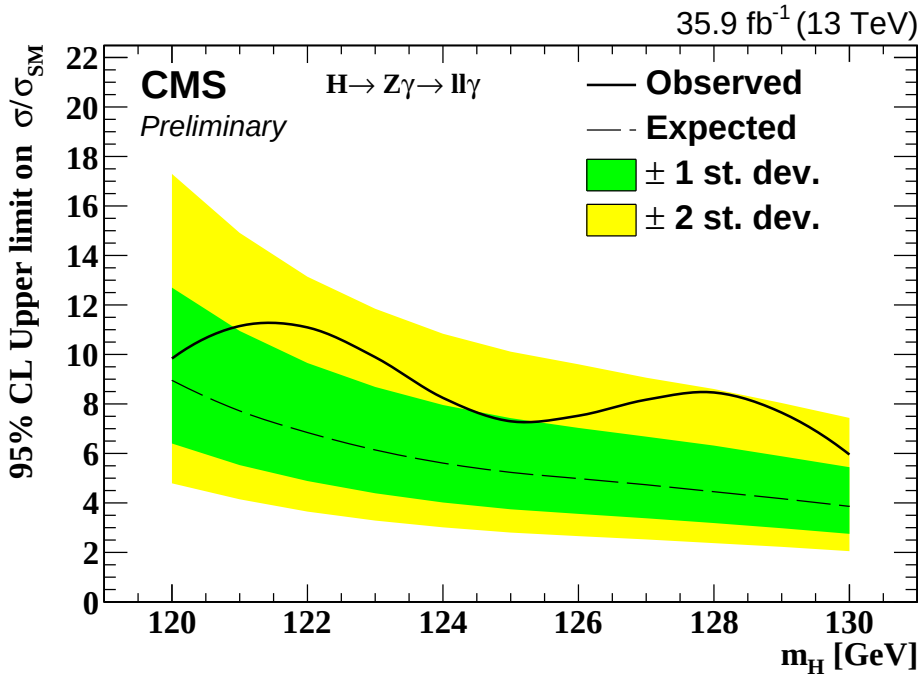

Figure 7: Exclusion limit, at 95% confidence level, on the cross section of $H \to Z\gamma \to \ell\ell\gamma$ as a function of the Higgs boson mass based on 35.9 fb^{-1} of data taken at 13 TeV.

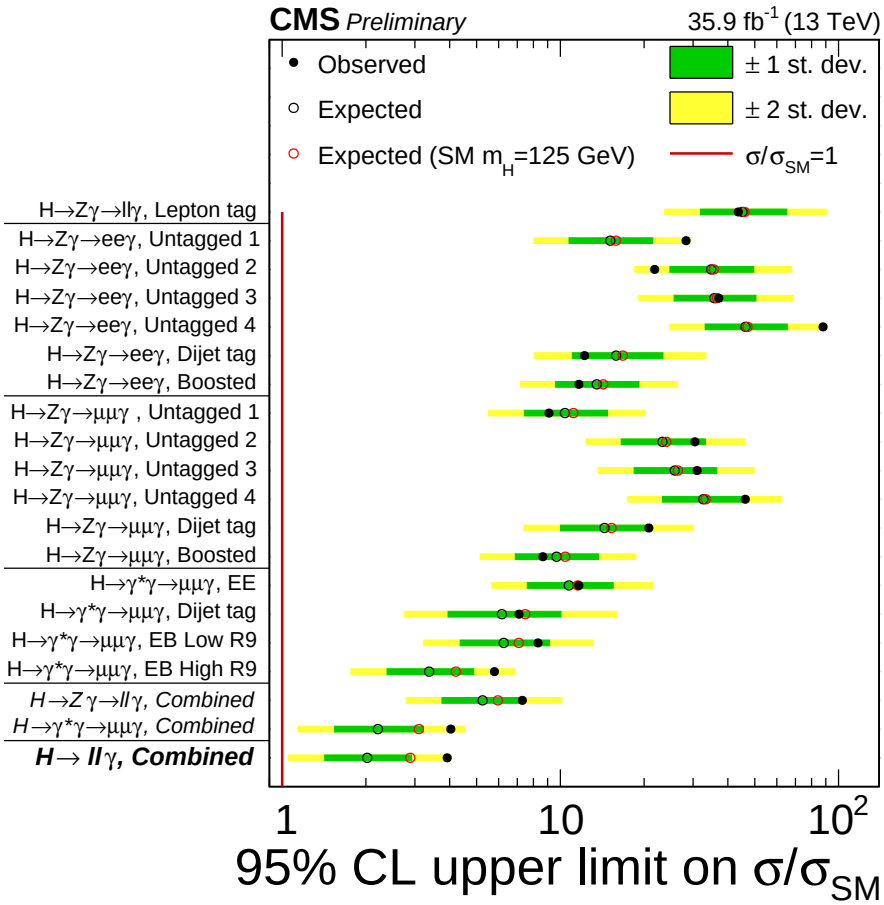

Figure 8: Exclusion limit, at 95% confidence level, on the cross section of H $\rightarrow \ell\ell\gamma$ for a SM Higgs boson of $m_{\mathrm{H}} = 125\,\mathrm{GeV}$. The upper limits of each analysis category, as well as their combinations, are shown. Black full (empty) circles show the observed (expected) limit. Red circles show the expected upper limit assuming a SM Higgs boson decaying to $\ell\ell\gamma$ decay channel.

References

[1] A. Abbasabadi, D. Bowser-Chao, D. A. Dicus, and W. W. Repko, "Radiative Higgs boson decays H $\to f f\gamma$", *Phys. Rev. D* **55** (1997) 5647, doi:10.1103/PhysRevD.55.5647, arXiv:hep-ph/9611209.

[2] Y. Sun, H. Chang, and D. Gao, "Higgs decays to $\gamma\ell^+\ell^-$ in the standard model", *JHEP* **05** (2013) 061, doi:10.1007/JHEP05(2013)061, arXiv:1303.2230.

[3] L. B. Chen, C. F. Qiao, and R. L. Zhu, "Reconstructing the 125 GeV SM Higgs boson through $\ell\bar{\ell}\gamma$", *Phys. Lett. B* **726** (2013) 306, doi:10.1016/j.physletb.2013.08.050, arXiv:1211.6058.

[4] G. Passarino, "Higgs boson production and decay: Dalitz sector", *Phys. Lett. B* **727** (2013) 424, doi:10.1016/j.physletb.2013.10.052, arXiv:1308.0422.

[5] A. Korchin and V. Kovalchuk, "Angular distribution and forward-backward asymmetry of the higgs-boson decay to photon and lepton pair", *Eur. Phys. J. C* **74** (2014) doi:10.1140/epjc/s10052-014-3141-7, arXiv:1408.0342.

[6] M. Bauer, M. Neubert, and A. Thamm, "LHC as an Axion Factory: Probing an Axion Explanation for $(g-2)_\mu$ with Exotic Higgs Decays", *Phys. Rev. Lett.* **119** (2017) doi:10.1103/PhysRevLett.119.031802, arXiv:1704.08207.

[7] LHC Higgs Cross Section Working Group Collaboration, "Handbook of LHC Higgs Cross Sections: 4. Deciphering the Nature of the Higgs Sector", doi:10.23731/CYRM-2017-002, arXiv:1610.07922.

[8] J. M. Campbell and R. Ellis, "MCFM for the Tevatron and the LHC", *Nucl. Phys. Proc. Suppl.* **205-206** (2010) 10, doi:10.1016/j.nuclphysbps.2010.08.011, arXiv:1007.3492.

[9] D. A. Dicus and W. W. Repko, "Calculation of the decay H $\to$ e$\bar{\text{e}}\gamma$", *Phys. Rev. D* **87** (2013) 077301, doi:10.1103/PhysRevD.87.077301, arXiv:1302.2159.

[10] D. A. Dicus and W. W. Repko, "Dalitz decay H $\to f\bar{f}\gamma$ as a background for H $\to \gamma\gamma$", *Phys. Rev. D* **89** (2014) 093013, doi:10.1103/PhysRevD.89.093013, arXiv:1402.5317.

[11] A. Firan and R. Stroynowski, "Internal conversions in Higgs decays to two photons", *Phys. Rev. D* **76** (2007) 057301, doi:10.1103/PhysRevD.76.057301, arXiv:0704.3987.

[12] ATLAS Collaboration, "Search for Higgs boson decays to a photon and a Z boson in pp collisions at $\sqrt{s}$ = 7 and 8 TeV with the ATLAS detector", *Phys. Lett. B* **732** (2014) 8, doi:10.1016/j.physletb.2014.03.015, arXiv:1402.3051.

[13] CMS Collaboration, "Search for a Higgs boson decaying into a Z and a photon in pp collisions at $\sqrt{s} = 7$ and 8 TeV", *Phys. Lett. B* **726** (2013) 587, doi:10.1016/j.physletb.2013.09.057, arXiv:1307.5515.

[14] CMS Collaboration, "Search for a Higgs boson decaying into $\gamma^*\gamma \to \ell\ell\gamma$ with low dilepton mass in pp collisions at $\sqrt{s} = 8$ TeV", *Phys. Lett. B* **753** (2016) 341, doi:10.1016/j.physletb.2015.12.039, arXiv:1507.03031.

[15] CMS Collaboration, "The CMS experiment at the CERN LHC", *JINST* **3** (2008) S08004, doi:10.1088/1748-0221/3/08/S08004.

[16] CMS Collaboration, "Particle-flow reconstruction and global event description with the CMS detector", *JINST* **12** (2017) P10003, doi:10.1088/1748-0221/12/10/P10003, arXiv:1706.04965.

[17] CMS Collaboration, "Performance of photon reconstruction and identification with the CMS detector in proton-proton collisions at $\sqrt{s} = 8$ TeV", *JINST* **10** (2015) P08010, doi:10.1088/1748-0221/10/08/P08010, arXiv:1502.02702.

[18] CMS Collaboration, "Measurement of the Inclusive W and Z Production Cross Sections in pp Collisions at $\sqrt{s} = 7$ TeV", *JHEP* **10** (2011) 132, doi:10.1007/JHEP10(2011)132, arXiv:1107.4789.

[19] CMS Collaboration, "Measurements of properties of the Higgs boson decaying into the four-lepton final state in pp collisions at $\sqrt{s} = 13$ TeV", *JHEP* **11** (2017) 047, doi:10.1007/JHEP11(2017)047, arXiv:1706.09936.

[20] M. Cacciari, G. P. Salam, and G. Soyez, "FastJet User Manual", *Eur. Phys. J. C* **72** (2012) 1896, doi:10.1140/epjc/s10052-012-1896-2, arXiv:1111.6097.

[21] J. Alwall et al., "The automated computation of tree-level and next-to-leading order differential cross sections, and their matching to parton shower simulations", *JHEP* **07** (2014) 079, doi:10.1007/JHEP07(2014)079, arXiv:1405.0301.

[22] P. Artoisenet et al., "A framework for Higgs characterisation", *JHEP* **11** (2013) 043, doi:10.1007/JHEP11(2013)043, arXiv:1306.6464.

[23] P. de Aquino and K. Mawatari, "Characterising a Higgs-like resonance at the LHC", in *Proceedings, 1st Toyama International Workshop on Higgs as a Probe of New Physics 2013 (HPNP2013): Toyama, Japan, February 13-16, 2013*. 2013. arXiv:1307.5607.

[24] T. Sjöstrand, S. Mrenna, and P. Z. Skands, "A brief introduction to PYTHIA 8.1", *Comput. Phys. Commun.* **178** (2008) 852, doi:10.1016/j.cpc.2008.01.036, arXiv:0710.3820.

[25] S. Alioli, P. Nason, C. Oleari, and E. Re, "NLO Higgs boson production via gluon fusion matched with shower in POWHEG", *JHEP* **04** (2009) 002, doi:10.1088/1126-6708/2009/04/002, arXiv:0812.0578.

[26] P. Nason and C. Oleari, "NLO Higgs boson production via vector-boson fusion matched with shower in POWHEG", *JHEP* **02** (2010) 037, doi:10.1007/JHEP02(2010)037, arXiv:0911.5299.

[27] NNPDF Collaboration, "Parton distributions for the LHC Run II", *JHEP* **04** (2015) 040, doi:10.1007/JHEP04(2015)040, arXiv:1410.8849.

[28] M. J. Oreglia, "A study of the reactions $\psi' \to \gamma\gamma\psi$". PhD thesis, Stanford University, 1980. SLAC Report SLAC-R-236, see Appendix D.

[29] A. L. Read, "Presentation of search results: The CL(s) technique", *J. Phys.* **G28** (2002) 2693–2704, doi:10.1088/0954-3899/28/10/313.

[30] T. Junk, "Confidence level computation for combining searches with small statistics", *Nucl. Instrum. Meth. A* **434** (1999) 435, doi:10.1016/S0168-9002(99)00498-2, arXiv:hep-ex/9902006.

[31] The ATLAS Collaboration, The CMS Collaboration, The LHC Higgs Combination Group Collaboration, "Procedure for the LHC Higgs boson search combination in Summer 2011", Technical Report CMS-NOTE-2011-005. ATL-PHYS-PUB-2011-11, CERN, Geneva, Aug, 2011.

[32] CMS Collaboration Collaboration, "CMS Luminosity Measurements for the 2016 Data Taking Period", Technical Report CMS-PAS-LUM-17-001, CERN, Geneva, 2017.

[33] A. D. Martin, W. J. Stirling, R. S. Thorne, and G. Watt, "Parton distributions for the LHC", *Eur. Phys. J. C* **63** (2009) 189, doi:10.1140/epjc/s10052-009-1072-5, arXiv:0901.0002.

[34] H. Lai et al., "New parton distributions for collider physics", *Phys. Rev. D* **82** (2010) 74024, doi:10.1103/PhysRevD.82.074024, arXiv:1007.2241.

[35] S. Alekhin et al., "The PDF4LHC Working Group Interim Report", (2011). arXiv:1101.0536.

[36] M. Botje et al., "The PDF4LHC Working Group Interim Recommendations", (2011). arXiv:1101.0538.